Numerical Modeling of Holmium-Doped Fluoride Fiber Lasers

Jianfeng Li, *Member, IEEE*, Laércio Gomes, and Stuart D. Jackson, *Member, IEEE*

***Abstract*— We combine all the known experimental demonstrations and spectroscopic parameters into a numerical model of the Ho^{3+}-doped fluoride glass fiber laser system. Core-pumped and cladding-pumped arrangements were simulated for all the population-bottlenecking mitigation schemes that have been tested, and good agreement between the model and the previously reported experimental results was achieved in most but not in all cases. In a similar way to Er^{3+}-doped fluoride glass fiber lasers, we found that the best match with measurements required scaled-down rate parameters for the energy transfer processes that operate in moderate to highly concentrated systems. The model isolated the dominant processes affecting the performance of each of the bottlenecking mitigation schemes and pump arrangements. It was established that pump excited-state absorption is the main factor affecting the performance of the core-pumped demonstrations of the laser, while energy transfer between rare earth ions is the main factor controlling the performance in cladding-pumped systems.**

***Index Terms*— Fiber lasers, fluoride glass, holmium lasers.**

I. Introduction

THERE is continuing strong interest in the development of high power 3 μm class fiber lasers for applications in defense, health and the environment. To date, fluoride glass fibers doped with rare earth ions such as erbium [1], holmium [2] and dysprosium [3] have been successfully used to create high power radiation at emission wavelengths approaching 3 μm. Erbium doped fluoride fiber lasers are currently the most convenient $\sim$3 μm fiber laser because high power diodes are readily available for the 975 nm absorption band of Er^{3+} which excites the upper laser level directly. As a result, an all-fiber erbium-doped ZBLAN fiber laser emitting 20.6 W at a Stokes limit superseding 35.4% slope efficiency at 2.825 μm has been reported [4]. Saturation of the laser output power, however, has been observed at high pump power and may limit further power scaling [4, 5]. On the other hand, holmium-based fiber lasers whilst demonstrating output power levels which are much lower compared to erbium-based fiber lasers nevertheless have shown high efficiency [6], high power [2] and broad tunability [7] and offer the opportunity, as a result of the longer fluorescence wavelength compared to erbium, to extend the emission from fiber lasers into the mid-infrared region [8]. The $^5I_6 \rightarrow {}^5I_7$ laser transition of Ho^{3+} encounters a population bottlenecking problem because the lifetime of the $^5I_6$ level (3.5 ms) is shorter than the lifetime of the $^5I_7$ level (12 ms) and in a similar way to the Er^{3+} system, Ho^{3+} requires some engineering of the laser process to create efficient emission.

There are a number of approaches to the reduction of the population in the longer-lived $^5I_7$ lower laser level. Cascading of the two laser transitions simultaneously i.e., the $^5I_6 \rightarrow {}^5I_7$ and $^5I_7 \rightarrow {}^5I_8$ transitions has been shown to be an effective way to deplete the $^5I_7$ population [9, 10]. A maximum two-transition output power of 3 W at a slope efficiency of 65% was achieved from a cascade Ho^{3+}-doped ZBLAN fiber laser when pumped at 1150 nm [9]. Quenching of the $^5I_7$ lifetime by Pr^{3+} co-doping has resulted in Watt-level output on the $^5I_6 \rightarrow {}^5I_7$ transition at slope efficiencies of 28% from core pumped fibers [6] and 32% from cladding pumped fibers [2] when pumped near 1100 nm and 1150 nm, respectively. Pump excited-state absorption (ESA) near 1150 nm has been successful in core-pumped arrangements with low and highly doped fibers generating slope efficiencies of 45% [11] and 4.3% [12], respectively. There have, however, been few reports detailing the theoretical aspects of Ho^{3+}-doped fluoride fiber lasers. Given the wide range of experimental demonstrations and spectroscopic parameters that are now available, a detailed and systematic analysis for each bottlenecking mitigation scheme relevant to Ho^{3+}-doped fluoride glass is necessary in order to establish limits and comparisons on the performance of these lasers.

In this investigation, a numerical model employing solution of the rate equations and the pump and signal field propagation equations was created which involves all the known energy transfer and transition processes relevant to the cascaded, Pr^{3+}-co-doped, and single transition Ho^{3+}-doped fluoride glass fiber lasers. The results from previously reported fiber laser demonstrations are compared with the model to test the validity of our approach. The bottlenecking mitigation schemes and important interionic processes affecting

Manuscript received November 15, 2011; revised January 15, 2012; accepted January 23, 2012. Date of current version March 6, 2012. This work was supported in part by the National Natural Science Foundation of China under Grant 61107037 and Grant 60925019, by the China Postdoctoral Science Special Foundation under Grant 201003693, by the China Postdoctoral Science Foundation under Grant 20090451417, and by the Fundamental Research Funds for the Central Universities under Grant ZYGX2009J053.

J. Li is with the School of Optoelectronic Information, State Key Laboratory of Electronic Thin Films and Integrated Devices, University of Electronic Science and Technology of China, Chengdu 610054, China, and also with the School of Physics, Institute of Photonics and Optical Science, University of Sydney, Sydney 2006, Australia (e-mail: lijianfeng@uestc.edu.cn).

L. Gomes is with the Center for Lasers and Applications, IPEN/CNEN-SP, São Paulo 05422-970, Brazil (e-mail: lgomes@ipen.br).

S. D. Jackson is with the School of Physics, Institute of Photonics and Optical Science, University of Sydney, Sydney 2006, Australia (e-mail: s.jackson@usyd.edu.au).

Color versions of one or more of the figures in this paper are available online at http://ieeexplore.ieee.org.

Digital Object Identifier 10.1109/JQE.2012.2188380

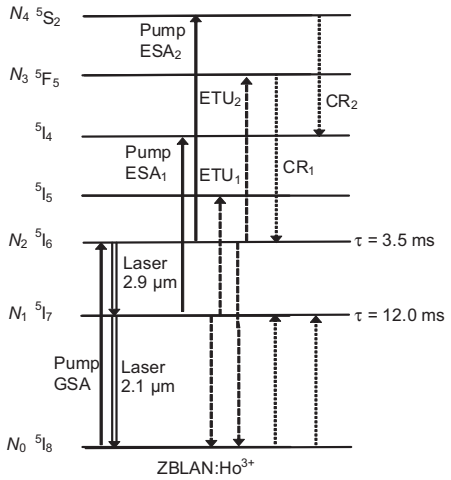

Fig. 1. Schematic diagram of the energy levels relevant to the cascade Ho^{3+}-doped ZBLAN fiber laser. The pump, energy transfer upconversion, and laser transitions are shown.

the laser performance for each system were then analyzed in detail.

II. Numerical Model

A. Cascade Ho^{3+}-Doped ZBLAN Fiber Lasers

Fig. 1 shows the energy-level scheme relevant to cascade Ho^{3+}-doped fluoride (ZBLAN) fiber lasers. Pump ground state absorption (GSA) at 1150 nm excites the Ho^{3+} ions to the $^5I_6$ level. ESA (labeled ESA_1 in Fig. 1) at 1150 nm excites the Ho^{3+} ions from the $^5I_7$ level to $^5I_4$ level and ESA (labeled ESA_2 in Fig. 1) at 1150 nm can also excite Ho^{3+} ions from the $^5I_6$ level to $^5S_2$ level. The relevant laser transition occurs between the $^5I_6$ and $^5I_7$ levels at a wavelength of $\sim$2.9 μm in ZBLAN glass. By cascading the $^5I_7 \rightarrow {}^5I_8$ laser transition at a wavelength of $\sim$2.1 μm, the lower laser $^5I_7$ level is depopulated quickly which mitigates the population bottleneck. The energy transfer upconversion (ETU) process (labeled ETU_1)$^5I_7$, $^5I_7 \rightarrow {}^5I_6$, $^5I_8$ is, in principle, useful for depletion of the lower laser level of the 2.9 μm transition because half of the excited ions can be theoretically upconverted to the upper $^5I_6$ laser level by ETU_1. The population density in the $^5I_6$ upper laser level, however, is depleted by a second ETU process (labeled ETU_2) $^5I_6$, $^5I_6 \rightarrow {}^5F_5$, $^5I_8$ that is detrimental to the $\sim$2.9 μm laser transition. In contrast to the Er^{3+}-doped ZBLAN glass system, the ETU_2 rate parameter is comparatively larger than the ETU_1 rate parameter in bulk Ho^{3+}-doped ZBLAN glass [13]. The Ho^{3+} dopant concentration in cascade laser systems, however, is generally chosen low enough to prevent a significant degree of ETU.

According to the energy levels shown in Fig. 1, the rate equations for the population densities $N_i(z, t)$ are given by

$$\frac{dN_4(z)}{dt} = R_{ESA2}(z) - W_{40}N_4(z)N_0(z) - \tau_4^{-1}N_4(z) \quad (1)$$

$$\frac{dN_3(z)}{dt} = W_{22}N_2^2(z) - W_{30}N_3(z)N_0(z) - \tau_3^{-1}N_3(z), \quad (2)$$

$$\frac{dN_2(z)}{dt} = R_{GSA}(z) + \beta_{32}\tau_3^{-1}N_3(z) + W_{30}N_3(z)N_0(z) + W_{40}N_4(z)N_0(z) - \tau_2^{-1}N_2(z) - 2W_{22}N_2^2(z) + W_{11}N_1^2(z) - R_{ESA2}(z) + R_{ESA1}(z) - R_{SE}(z), \quad (3)$$

$$\frac{dN_1(z)}{dt} = R_{SE}(z) + \sum_{i=2,3}\left[\beta_{i1}\tau_i^{-1}N_i(z)\right] + W_{30}N_3(z)N_0(z) + W_{40}N_4(z)N_0(z) - 2W_{11}N_1^2(z) - R_{ESA1}(z) - \tau_1^{-1}N_1(z) - R_{SE1}(z), \quad (4)$$

$$N_{Ho} = \sum_{i=0,\ldots,4} N_i, \quad (5)$$

where τ_i represents the intrinsic lifetimes of the energy levels at low dopant concentration and includes radiative decay as well as decay from multiphonon relaxation. β_{ij} represents the branching ratios for decay from level i to a lower level j. The values for τ_i and β_{ij} can be found in [13]. W_{11} and W_{22} represent the parameters for ETU from the $^5I_7$ and $^5I_6$ energy levels, respectively. W_{30} and W_{40} represent the cross relaxation (labeled CR_1 and CR_2) parameters from the $^5F_5$ and $^5S_2$ energy levels, respectively. The GSA, ESA_1 and ESA_2 rates R_{GSA}, R_{ESA1} and R_{ESA2} can be defined as

$$R_{GSA}(z) = \frac{\lambda_p\Gamma_p\sigma_{GSA}}{hcA_{eff}}N_0(z)\left[P_P^+(z) + P_P^-(z)\right], \quad (6)$$

$$R_{ESA1}(z) = \frac{\lambda_p\Gamma_p\sigma_{ESA1}}{hcA_{eff}}N_1(z)\left[P_P^+(z) + P_P^-(z)\right], \quad (7)$$

$$R_{ESA2}(z) = \frac{\lambda_p\Gamma_p\sigma_{ESA2}}{hcA_{eff}}N_2(z)\left[P_P^+(z) + P_P^-(z)\right], \quad (8)$$

where λ_p denotes the pump wavelength. Γ_p denotes the power-filling factor for the pump light, whose value is 1.0 for core pumped fiber lasers or can be calculated from the ratio of the active core area to the pump core area for cladding pumped fiber lasers. σ_{GSA} represents the GSA cross-section at the pump wavelength. σ_{ESA1} and σ_{ESA2} represent the ESA_1 and ESA_2 cross sections at the pump wavelength, respectively. h denotes Planck's constant and c is the speed of light. A_{eff} represents the effective cross-section area of fiber core. $P_p^+(z, t)$ and $P_p^-(z, t)$ represent the forward and backward propagating pump power, respectively. The stimulated-emission rates R_{SE21} and R_{SE10} for the 2.9 μm and 2.1 μm emissions are given by

$$R_{SE21}(z) = \frac{\lambda_{s21}\Gamma_{s21}\sigma_{se21}}{hcA_{eff}}\left[b_2N_2(z) - b_1N_1(z)\right]\left[P_{s21}^+(z) + P_{s21}^-(z)\right], \quad (9)$$

$$R_{SE10}(z) = \frac{\lambda_{s10}\Gamma_{s10}\sigma_{se10}}{hcA_{eff}}\left[b_{11}N_1(z) - b_0N_0(z)\right]\left[P_{s10}^+(z) + P_{s10}^-(z)\right], \quad (10)$$

where λ_{s21} and λ_{s10} denote the signal (i.e., laser) wavelength for the $^5I_6 \rightarrow {}^5I_7$ and $^5I_7 \rightarrow {}^5I_8$ transitions, respectively. Γ_{s1} and Γ_{s2} denote the power filling factors for the corresponding signal. The signals are assumed a Gaussian distribution with radius $\omega_0 = r_{core}(0.65+1.619V^{-1.5}+2.876V^{-6})$, and thus Γ_{s1} and Γ_{s2} can be calculated using $1\text{-}\exp[-2(r_{core}/\omega_0)^2]$ with the core radius of fiber r_{core} and the normalized frequency

V. σ_{se21} and σ_{se10} are the stimulated-emission cross-section of the laser emission at output wavelengths λ_{s21} and λ_{s10}, respectively. b_1 and b_2 are Boltzmann factors of the $^5I_6$ and $^5I_7$ Stark levels for the $\sim$3 μm transition. b_{11} and b_0 are the Boltzmann factors of the $^5I_7$ and $^5I_8$ Stark levels for the $\sim$2.1 μm transition. The use of the Boltzmann factors in the calculation of the population inversion has been previously used in the rate equation modeling of fiber lasers, however, the standard approach to calculate the population inversion of laser transitions involving the ground state engages the use of the emission and absorption cross sections at a given emission wavelength and the relevant population densities. The use of Boltzmann factors in the present case is an approximation which we apply to both transitions. $P^+_{s21}(z, t)$ and $P^-_{s21}(z, t)$ denote the forward and backward propagating signal powers along the z direction for the $\sim$3 μm emission, respectively. $P^+_{s10}(z, t)$ and $P^-_{s10}(z, t)$ denote the forward and backward propagating signal powers along the z direction for $\sim$2.1 μm emission, respectively. The power evolution along the fiber of the pump light and the signal light can be obtained by

$$\pm\frac{dP^{\pm}_{s21}(z)}{dz} = \Gamma_{s21}\sigma_{se21}[b_2N_2(z) - b_1N_1(z)] \times P^{\pm}_{s21}(z) - \alpha_{s21}P^{\pm}_{s21}(z), \quad (11)$$

$$\pm\frac{dP^{\pm}_{s10}(z)}{dz} = \Gamma_{s10}\sigma_{se10}[b_{11}N_1(z) - b_0N_0(z)] \times P^{\pm}_{s10}(z) - \alpha_{s10}P^{\pm}_{s10}(z), \quad (12)$$

$$\pm\frac{dP^{\pm}_{p}(z)}{dz} = -\Gamma_p[\sigma_{GSA}N_0(z) + \sigma_{ESA1}N_1(z) + \sigma_{ESA2}N_2(z)] \times P^{\pm}_{p}(z) - \alpha_p P^{\pm}_{p}(z), \quad (13)$$

where α_p represents the background loss coefficients of pump light, α_{s21} and α_{s10} represent the background loss coefficients of the 3 μm and 2.1 μm emissions, respectively.

The pump power and laser power at both fiber ends are subjected to the boundary conditions:

$$P^+_p(0) = R_{p1}P^-_p(0) + P_{\text{launched}}, \quad (14)$$

$$P^-_p(L) = R_{p2}P^+_p(L), \quad (15)$$

$$P^+_{s21}(0) = Rf1_{21}P^-_{s21}(0), \quad (16)$$

$$P^-_{s21}(L) = Rf2_{21}P^+_{s21}(L), \quad (17)$$

$$P^+_{s10}(0) = Rf1_{10}P^-_{s10}(0), \quad (18)$$

$$P^-_{s10}(L) = Rf2_{10}P^+_{s10}(L), \quad (19)$$

where R_{p1} and R_{p2} are the input and output mirror reflectivites at the pump wavelength, respectively and P_{launched} is the launched pump power into the cladding of the fiber. L is the length of the fiber. $Rf1_{21}$ and $Rf2_{21}$ are the reflectivities of the front mirror and output mirror for 3-μm emission, respectively. $Rf1_{10}$ and $Rf2_{10}$ are the reflectivities of the front mirror and output mirror for 2.1 μm emission, respectively. The population density rate equations can be solved with a routine suited to solving Stiff rate equations, and the pump and laser power can be computed with a longitudinal discretization of the active medium of elements of equal length using the fourth-order Runge-Kutta method.

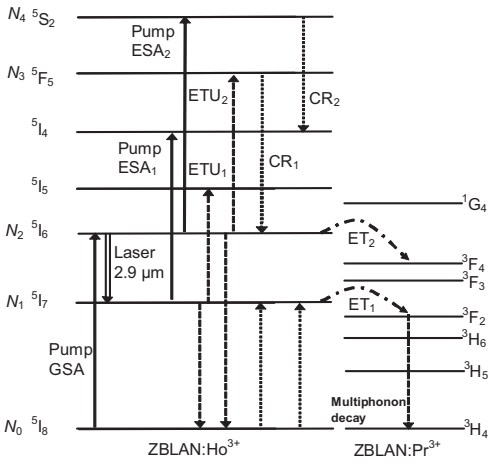

Fig. 2. Schematic diagram of the energy levels relevant to the Ho^{3+}-Pr^{3+} co-doped ZBLAN fiber laser. The pump, energy transfer, and laser transitions are shown.

Note that the above rate equation approach relies on rapid energy transfer between Ho^{3+} ions which allows the use of single values for the energy level populations. At low (i.e., <1 mol.%) Ho^{3+} concentration, ET obeys the Inokuti-Hirayama model which results in non-exponential decay times and the distribution of excited Ho^{3+} ions may be spatially non-uniform. Such conditions are complicated to model and the results from the current model for systems involving low Ho^{3+} concentrations can be considered as first approximations.

B. Ho^{3+}, Pr^{3+}-Co-Doped ZBLAN Fiber Lasers

Fig. 2 shows the energy-level scheme for Ho^{3+}, Pr^{3+}-co-doped ZBLAN fiber lasers. Co-doping with Pr^{3+} forces efficient energy transfer (labeled ET_1) from Ho^{3+} to Pr^{3+} resulting in the $^5I_7$ lower laser level being effectively depopulated. Fast decay to the ground state by multiphonon decay within Pr^{3+} reduces ground state bleaching and enables efficient CW operation of the laser. The ET_1 process, however, reduces any effects from energy recycling by ETU_1.

According to the energy level diagram shown in Fig. 2, the change to the rate equations that take account of Pr^{3+} co-doping are given by

$$\frac{dN_2(z)}{dt} = R_{GSA}(z) + \beta_{32}\tau_3^{-1}N_3(z) + W_{30}N_3(z)N_0(z) + W_{40}N_4(z)N_0(z) - \tau_2^{-1}N_2(z) - 2W_{22}N_2^2(z) + W_{11}N_1^2(z) - R_{ESA2}(z) + R_{ESA1}(z) - R_{SE}(z) - W_2N_2(z)N_{\text{Pr}}, \quad (20)$$

$$\frac{dN_1(z)}{dt} = R_{SE}(z) + \sum_{i=2,3}\left[\beta_{i1}\tau_i^{-1}N_i(z)\right] + W_{30}N_3(z)N_0(z) + W_{40}N_4(z)N_0(z) - 2W_{11}N_1^2(z) - R_{ESA1}(z) - \tau_1^{-1}N_1(z) - W_1N_1(z)N_{\text{Pr}}, \quad (21)$$

where W_1 and W_2 represent the parameters for ET from the $^5I_7$ and $^5I_6$ energy levels, respectively, the value of which changes with the Ho^{3+} and Pr^{3+} concentrations. Eqs. (10) and (12), and the boundary conditions (18) and (19) relating to the $^5I_7 \rightarrow {}^5I_8$ laser transition are not necessary for this case.

TABLE I
CONSTANT SPECTROSCOPIC PARAMETERS USED IN THE SIMULATIONS [13]

Parameters	Values
τ_1	12.0 ms
τ_2	3.5 ms
τ_3	50 μs
τ_4	290 μs
β_{21}, β_{20}	0.09, 0.91
β_{32}, β_{31}, β_{30}	0.05, 0.18, 0.77

C. Singly Resonant Ho^{3+}-Doped ZBLAN Fiber Lasers

In core pumped laser fiber systems, ESA_1 can de-populate the $^5I_7$ level as a result of the high pump intensity sufficiently enough to create a population inversion. Under this condition, the population densities $N_2(z)$ and $N_1(z)$ can be calculated from:

$$\begin{aligned}\frac{dN_2(z)}{dt} &= R_{GSA}(z) + \beta_{32}\tau_3^{-1}N_3(z) \\ &\quad + W_{30}N_3(z)N_0(z) + W_{40}N_4(z)N_0(z) - 2W_{22}N_2^2(z) \\ &\quad + W_{11}N_1^2(z) - \tau_2^{-1}N_2(z) - R_{ESA2}(z) \\ &\quad + R_{ESA1}(z) - R_{SE}(z), \qquad (22)\end{aligned}$$

$$\begin{aligned}\frac{dN_1(z)}{dt} &= R_{SE}(z) + \sum_{i=2,3}\left[\beta_{i1}\tau_i^{-1}N_i(z)\right] \\ &\quad + W_{30}N_3(z)N_0(z) + W_{40}N_4(z)N_0(z) \\ &\quad - 2W_{11}N_1^2(z) - R_{ESA1}(z) - \tau_1^{-1}N_1(z). \qquad (23)\end{aligned}$$

III. RESULTS

In order to estimate the versatility and accuracy of the numerical model, we compared the published experimental measurements with the theoretically generated results for a variety of pump, resonator and fiber configurations. Table I lists the consistent spectroscopic parameters for the different systems including the lifetimes τ_i and branching ratios β_{ij}.

A. Cascade Ho^{3+}-Doped ZBLAN Fiber Lasers

Firstly, the calculation from our model was compared with the core pumped low concentration cascade laser experiment described in [9]. The fiber used in [9] was identical to that reported in [10]. In the simulation, the fiber specific parameters were: cladding diameter = 250 μm with a core diameter = 10 μm and $NA = 0.26$. The propagation loss α_{s21} and α_{s10} in the 3 μm and 2 μm bands were 70 dB/km and 10 dB/km, respectively. The Ho^{3+} concentration N_{Ho} was 2.2×10^{25} m^{-3}. The fiber length in the experiment was 2.5 m to ensure a pump absorption efficiency of >90%. The reflection coefficients $Rf1_{21}$ and $Rf1_{10}$ were 99%. The reflection coefficients $Rf2_{21}$ and $Rf2_{10}$ related to Fresnel reflection and were approximately 4%.

According to [14], the parameters for ETU and CR appear to be smaller in Er^{3+}-doped ZBLAN fibers compared to Er^{3+}-doped bulk ZBLAN glasses. We believe the same situation may also relate to the holmium system. In the simulation, the energy transfer parameters were classified into two groups i.e., Strongly Interacting (SI) and Weakly Interacting (WI). For the SI rate parameter case, the values for W_{11}, W_{22}, W_{30} as well as W_{40} were taken from the measurements in bulk glasses [13]. By simulating the inband diode pumped 2.1 μm Ho^{3+}-doped fiber laser in [15] and [16], the value of W_{11} was determined to be 12 times lower than that in the bulk glass because the W_{11} process is the only ET process that affects the threshold pump power in this system. As we show in the calculations below, for the WI rate parameter case, the values for W_{11}, W_{22}, W_{30} as well as W_{40} were all estimated to be 12 times lower than the bulk glass values. The values of the WI and SI rate parameters are listed at Table II.

TABLE II
ENERGY TRANSFER PARAMETERS FOR THE STRONGLY INTERACTING [13] AND WEAKLY INTERACTING CONDITIONS

Parameters	Value (SI) [m^3 s^{-1}]	Value (WI) [m^3 s^{-1}]
W_{11}	7×10^{-24}	0.53×10^{-24}
W_{22}	5×10^{-23}	0.42×10^{-23}
W_{30}	1.0×10^{-23}	0.83×10^{-24}
W_{40}	2×10^{-24}	0.17×10^{-25}

The wavelength of the pump transition, $^5I_6 \rightarrow {}^5I_7$ laser transition, and $^5I_7 \rightarrow {}^5I_8$ laser transition was 1150 nm, 2920 nm and 2060 nm, respectively [9]. The GSA and ESA cross-sections at 1150 nm i.e., σ_{GSA}, σ_{ESA1} and σ_{ESA2} were 1.85×10^{-21} cm^2 [2], 0.4×10^{-21} cm^2[17] and 0.15×10^{-21} cm^2 [17], respectively. Fig. 3 shows the measured Ho^{3+} fluorescence cross-section for the 2 μm fluorescence band and 3 μm fluorescence band for Ho^{3+}(2 mol%)-doped ZBLAN excited by a pulsed laser at 1151 nm (13 mJ, 4 ns, 10 Hz) measured at T = 300 K. The emission cross-section for $^5I_7 \rightarrow {}^5I_8$ transition at a wavelength of 2060 nm was approximately 4.0×10^{-21} cm^2.

The measured emission cross-section of Ho^{3+}(2 mol%)-doped ZBLAN glass in the 2 μm band and 3 μm band are shown in Fig. 3(a) and 3(b), respectively. The measured absorption cross-section of Ho^{3+}(2 mol%)-doped ZBLAN glass in 2 μm band is shown in Fig. 3(c). In order to calculate the average Boltzmann factors for the $^5I_7 \rightarrow {}^5I_8$ transition, the $^5I_7 \rightarrow {}^5I_8$ emission spectrum was decomposed into three Gaussian functions, whose peaks are located at 1947 nm, 2013 nm and 2070 nm, as shown in Fig. 3(a). Assuming that the $^5I_7 \rightarrow {}^5I_8$ transition originated from the bottom of the $^5I_7$ manifold, we can obtain the position of the main sub-levels within the $^5I_8$ manifold, which were derived from the relation

$$\left(\frac{1}{\lambda_1} - \frac{1}{\lambda_i}\right) \times 10^7 \text{cm}^{-1} = E_i, \qquad (24)$$

where $i = 2$ and 3. Using the fitted peaks, $\lambda_1 = 1947$ nm, $\lambda_2 = 2013$ nm and $\lambda_3 = 2070$ nm, the positions of the $^5I_8$ sub-levels were determined to be $E_1 = 0$ cm^{-1} (1), $E_2 = 168$ cm^{-1} (2), and $E_3 = 305$ cm^{-1} (3). The calculated Boltzmann factors were therefore 0.596 (1), 0.266 (2) and 0.138 (3) at 300 K. Using the same analysis, the position of the sub-level (1) of the $^5I_7$ multiplet is given by the relation

$$E_1 = \frac{1}{\lambda_1} \times 10^7 \text{ cm}^{-1} = 5136 \text{ cm}^{-1}. \qquad (25)$$

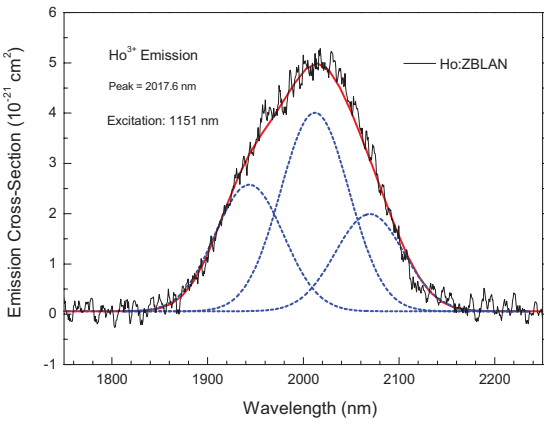

(a)

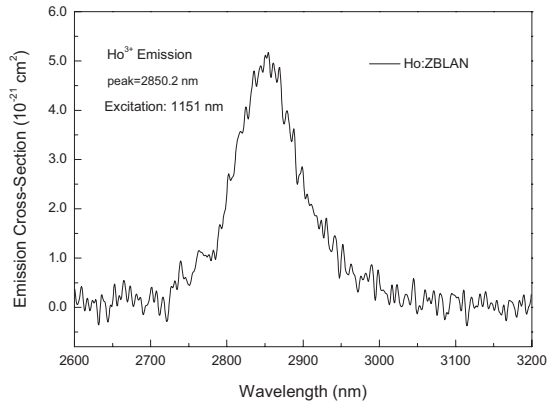

(b)

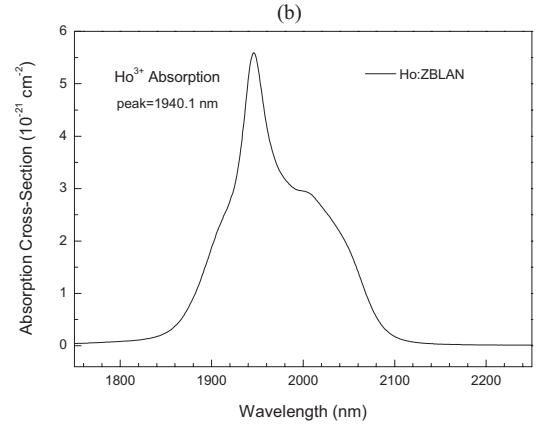

(c)

Fig. 3. Emission cross-section for Ho^{3+}(2 mol%)-doped ZBLAN in the (a) 2 μm band with three Gaussian function decomposition (broken lines), (b) 3 μm band excited by pulsed laser at 1151 nm (13 mJ, 4 ns, 10 Hz), and (c) absorption cross-section for Ho^{3+}(2 mol%)-doped ZBLAN in the 2 μm band measured at T = 300 K using a Cary 5000 spectrophotometer. The cross-section was taken using the relation $\sigma(\lambda)=(2.303 \times OD(\lambda)/(N \times d))$, where $OD(\lambda)$ is the optical density of measured spectrum, N is the Ho^{3+} concentration (2 mol%) equals to 3.05×10^{20} ions cm^{-3} and d is the sample thickness ($d = 0.51$ cm). The Gaussians peaks in (a) are located at 1947 nm (g_1), 2013 nm (g_2), and 2070 nm (g_3).

We can re-calculate the position of the three main $^5I_7$ sub-levels based on the values provided in [13] giving the location of the levels as 5136 cm^{-1}, 5350 cm^{-1}, and 5544 cm^{-1} and Boltzmann population factors 0.667, 0.239 and 0.094, respectively. Hence laser emission at 2070 nm corresponds to the transition $^5I_7$ sub-level (1) $\rightarrow$ $^5I_8$ sub-level (3) and the

TABLE III
COMPARISON OF THE SIMULATED RESULTS AND PUBLISHED EXPERIMENTAL RESULTS FROM [9]

	WI	SI	Expt
2.92 μm η_s [%]	31%	31%	30%
P_{th} [W]	0.09	0.25	~0.1
P_{out} [W]	1.41	1.36	1.4
2.06 μm η_s [%]	36%	36%	35%
P_{th} [W]	0.13	0.3	~0.13
P_{out} [W]	1.63	1.55	1.6

population factors are $b_{11} = 0.667$ and $b_0 = 0.138$. The $^5I_6 \rightarrow$ $^5I_7$ transition at a wavelength of 2.92 μm was assumed to originate from the lowest sub-level of the $^5I_6$ multiplet located at 8751 cm^{-1} with $b_2 = 1$ and terminate on the second Stark level of the $^5I_7$ manifold. The corresponding Boltzmann factors b_2/b_1 and emission cross-section are 1/0.239 and 1.5×10^{-21} cm^2, respectively, as shown in Fig. 3(b).

Fig. 4(a) shows the calculated laser output power using the WI and SI parameters for emission at 2.92 μm and the total laser output power for emission at 2.92 μm and 2.06 μm combined as a function of the launched pump power. Table III lists the calculated slope efficiency η_s, threshold power P_{th} and output power P_{out} at the launched pump power of 4.8 W for the SI and WI rate parameter regimes. Good agreement between the experiment and the numerical results using the WI rate parameter was achieved which valiates the use of the scaled-down rate parameters. Note that the main difference between the results using the WI rate parameters and the SI rate parameters is in the values of the threshold power and output power but the difference is small because of the low dopant concentration.

To investigate the influence of the fiber propagation loss on laser performance, the slope efficiency and threshold pump power as a function of propagation loss α_{s21} and α_{s10} across the range 10 dB/km to 500 dB/km was calculated. For variable α_{s21} and fixed α_{s10} (at 10 dB/km), the slope efficiency of the 2.92 μm output decreased linearly from 32% to 25.6% and the threshold pump power increased slightly from 0.087 W to 0.12 W, whilst the slope efficiency for emission at 2.06 μm decreased linearly from 36.7% to 34.9% and threshold pump power remained essentially unchanged. For variable α_{s10} and fixed α_{s21} of 70 dB/km, the slope efficiency and threshold pump power for 2.92 μm emission were essentially unchanged while the slope efficiency for emission at 2.06 μm decreased linearly from 36.5% to 26.4% and threshold pump power increased slightly from 0.13 W to 0.17 W with increasing α_{s10} to 500 dB/km.

To isolate the important transitions affecting the performance of the laser in this core-pumped cascade arrangement, the rates of GSA, ESA_1, ESA_2, ETU_1, ETU_2, CR_1, CR_2, SE_{21} and SE_{10} at the fiber output end were calculated as a function of the launched pump power, as shown in Fig. 5(a). GSA increases quickly with increasing absorbed pump power and no ground state bleaching occurs. Owing to the fast quenching

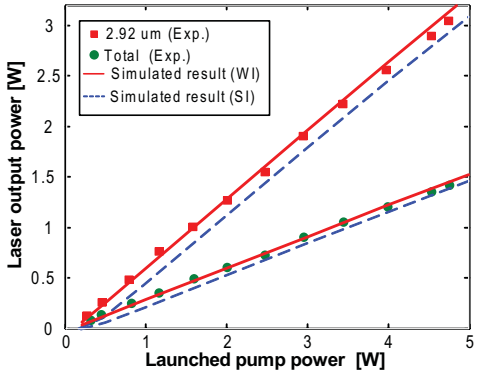

Fig. 4. Measured and calculated output power as a function of the launched pump power.

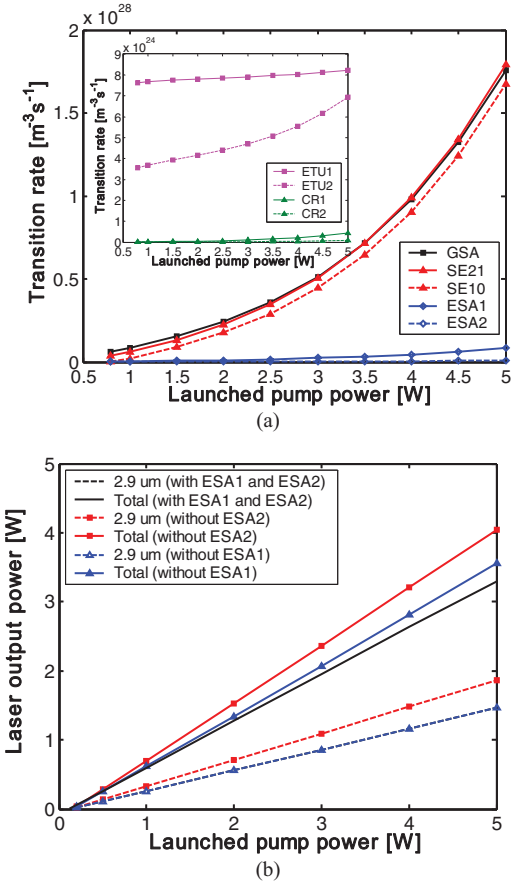

Fig. 5. (a) Calculated rates of GSA, ESA_1, ESA_2, ETU_1, ETU_2, CR_1, CR_2, SE_{21}, and SE_{10} at the output end of the fiber as a function of the launched pump power. (b) Calculated output power as a function of the launched pump power without ESA_1 or ESA_2.

of the population density in the $^5I_7$ level due to the high rate of SE_{10}, ESA_1 from this level has a rate that is ~10% the rate of GSA. Moreover, the rates of ETU_1, ETU_2, CR_1, and CR_2 are three orders of magnitude smaller than GSA as a result of the reduced rate parameters and low dopant concentration [see inset to Fig.5(a)], which suggests that these process have little affect on laser performance. To understand how ESA_1 and ESA_2 affect the performance of the laser, the calculated laser characteristic without the inclusion of ESA_2 or ESA_1 is shown

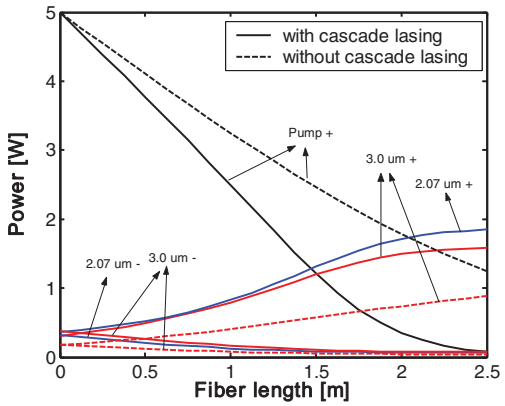

Fig. 6. Calculated forward and backward propagating pump and laser power distributions with or without cascade lasing along the fiber at 5 W of launched power.

in Fig. 5(b). The slope efficiencies for 2.92 μm emission and combined 2.92 μm and 2.06 μm output without ESA_2 were 38% and 83% respectively. These values are higher by 7% and 17% respectively compared to the original calculation demonstrating that ESA_2 seriously affects the performance of both laser transitions. The slope efficiency for the output at 2.92 μm without ESA_1 was nearly identical to the original calculation while the slope efficiency was 8% higher for 2.06 μm emission, demonstrating that ESA_1 primarily affects the performance of the output at 2.06 μm. As we show in more detail later, the ESA_1 process can de-populate the lower $^5I_7$ laser level for single $^5I_7 \rightarrow {}^5I_8$ transition lasing however, the output power is comparatively lower as shown in Fig. 6 which shows the intracavity power characteristics along the fiber length at a launched pump power of 5 W with or without cascade lasing. This result can be used to understand the mechanism behind the operation of core pumped singly Ho^{3+} doped ZBLAN fiber lasers [11].

To compare the performance between core pumped and cladding pumped cascade systems, we simulated our latest demonstration of a cladding-pumped cascade fiber laser that had a Ho^{3+} dopant concentration of 1.2 mol.% [8] using the model. In the simulation, the fiber specific parameters were: D-shape cladding diameter = 125 μm with a core diameter = 10 μm and $NA = 0.16$. The propagation loss α_{s21} and α_{s10} in the 3 μm and 2 μm bands were 100 dB/km and 50 dB/km, respectively. The Ho^{3+} concentration N_{Ho} was $1.65\times10^{26}\text{m}^{-3}$. The Boltzmann factors b_2/b_1 and emission cross-section relative to 3.0 μm are 1/0.18 and 0.6×10^{-21} cm^2, respectively. The Boltzmann factors b_{11}/b_0 and emission cross-section relative to 2.07 μm were 0.667/0.138 and 3×10^{-21} cm^2, respectively. The fiber length in the experiment was 10 m to ensure a pump absorption efficiency of >95%. The reflection coefficients $Rf1_{21}$ and $Rf1_{10}$ were 99% and 60%, respectively. The reflection coefficients $Rf2_{21}$ and $Rf2_{10}$ related to Fresnel reflection and were approximately 4%. The values for W_{11}, W_{22}, W_{30} and W_{40} for SI and WI regimes are listed in Table IV.

The experimental and calculated laser characteristic for 3.0 μm and 2.07 μm emission are shown in Fig. 7. Table V

TABLE IV
ENERGY TRANSFER PARAMETERS FOR THE STRONGLY INTERIONIC AND WEAKLY INTERIONIC CONDITIONS

Parameters	Value (SI) [m^3 s^{-1}]	Value (WI) [m^3 s^{-1}]
W_{11}	2.1×10^{-23}	1.75×10^{-24}
W_{22}	1.8×10^{-22}	1.5×10^{-23}
W_{30}	5.0×10^{-23}	4.17×10^{-24}
W_{40}	1×10^{-23}	8.3×10^{-25}

TABLE V
COMPARISON OF THE SIMULATED RESULTS AND PUBLISHED EXPERIMENTAL RESULTS FROM [9]

	WI	SI	Expt
3.0 μm η_s[%]	27%	27%	12.4%
P_{th} [W]	0.3	1.1	0.26
2.07 μm η_s[%]	34%	11.2%	4.3%
P_{th} [W]	2.0	7	2.6

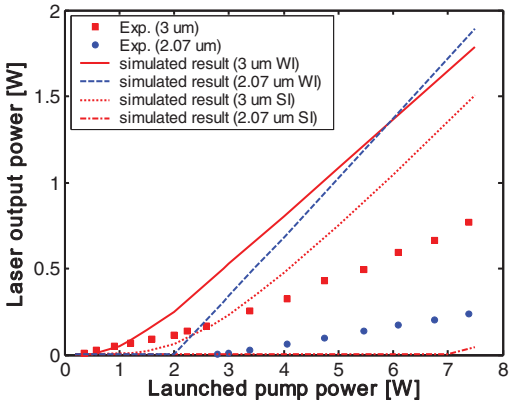

Fig. 7. Measured and calculated output power as a function of the launched pump power for the case of the cladding-pumped cascade fiber laser reported in [8].

lists the calculated slope efficiency η_s and threshold power P_{th} and output power P_{out} for the SI or WI rate parameter regimes.

It is observed that the calculated thresholds using WI parameters for 3.0 μm and 2.07 μm emissions are much closer to the experimental result compared with the results using SI parameters, however, the calculated slope efficiencies are substantially higher than the measurements. The experimental slope efficiencies are dependent on a number of fiber parameters including background loss of the pump or laser light and the quality of the fiber facets. When all inter-ionic and ESA processes in the model were switched off, agreement with the experimental results could not be reached. Clearly, an issue is at work here and we are currently investigating the source of the problem.

Compared with the calculations presented in Fig. 4, the calculated thresholds for emission at 3.0 μm and 2.07 μm in the cladding pumped arrangement were increased to 0.35 W and 2.0 W, respectively. The calculated slope efficiencies for 3.0 μm emission and the total output were 4% and 5%

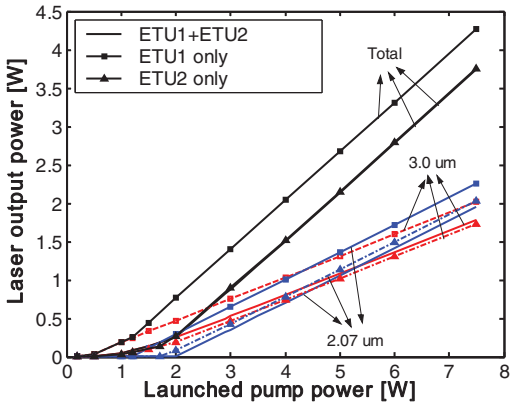

Fig. 8. Calculated output power as a function of the launched pump power for a variety of ETU conditions.

TABLE VI
COMPARISON OF THE SIMULATED RESULTS FOR ETU_1+ETU_2, ETU_2 ONLY AND ETU_1 ONLY IN CLADDING CASCADE SYSTEM

	ETU_1+ETU_2	ETU_1 only	ETU_2 only
3.0 μm η_s[%]	27%	27%	27%
P_{th} [W]	0.35	0.15	0.35
P_{out} [W]	1.72	1.94	1.66
2.07 μm η_s[%]	34%	34%	34%
P_{th} [W]	2.0	1.2	1.7
P_{out} [W]	1.87	2.16	1.95

lower than those presented in Fig. 4, respectively. Higher fiber loss due to the longer length and higher energy transfer upconversion rate parameters due to the higher concentration were main reasons leading to the reduced performance. Note that the rates of ESA_1 and ESA_2 in the cladding pumped system are negligibly small as a result of the low pump intensity. To isolate the effects of ETU_1 and ETU_2 on the laser performance, the calculated laser characteristic curves without ETU_1 or ETU_2 are shown in Fig. 8. With ETU_2 operating only, the slope efficiencies for 3.0 μm emission, 2.07 μm emission, and the total output are same as those when both ETU_1 and ETU_2 are present but the output power for 3.0 μm emission was comparatively lower and 2.07 μm emission comparatively higher for the same launched pump power which indicates that ETU_1 is beneficial for 3.0 μm emission but detrimental for 2.07 μm emission. With ETU_1 operating only, the slope efficiencies for each emission, and threshold power for 2.07 μm emission were identical to the characteristics without ETU_1, but the threshold power for 3.0 μm emission decreased to 0.15 W. The output power for each laser was higher by approximately 15% for the same launched pump power suggesting that ETU_2 is detrimental to both 3.0 μm and 2.07 μm transitions.

Fig. 9 shows the evolution of the intracavity power along the fiber at the launched pump power of 7.4 W with or without cascade lasing. It is observed that 3 μm emission can occur without cascade lasing although the output power is lower, which suggests that ETU_1 plays an important role

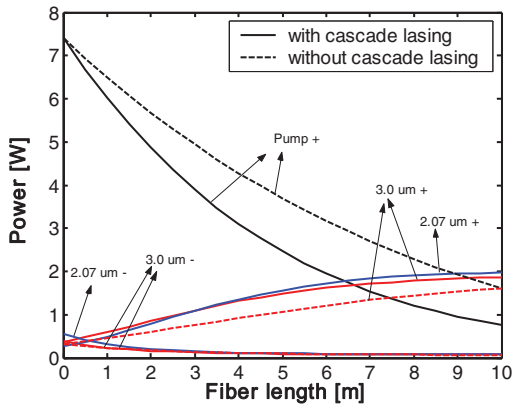

Fig. 9. Calculated forward and backward propagating pump and laser power distributions with or without cascade lasing along the fiber at 5 W of launched power.

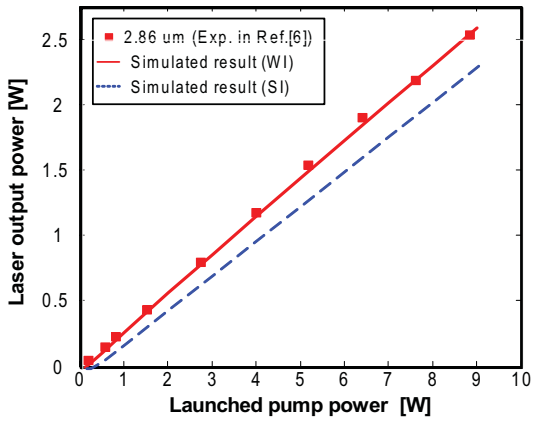

(a)

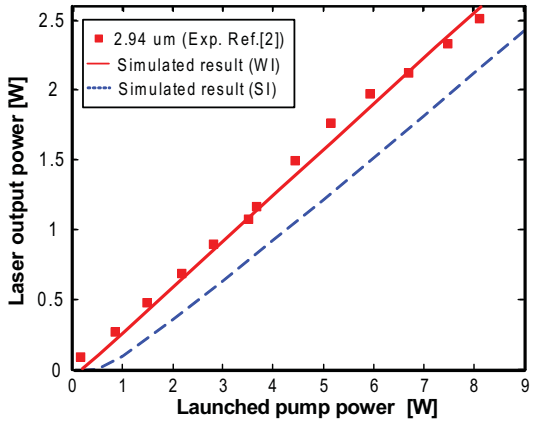

(b)

Fig. 10. Measured and calculated output power as a function of the launched pump power for (a) core-pumped and (b) cladding-pumped Ho^{3+}, Pr^{3+}-co-doped system.

depopulating the $^5I_7$ level in cladding pumped systems not employing cascade lasing.

B. Ho^{3+}, Pr^{3+}-Co-Doped ZBLAN Fiber Lasers

Compared with the cascade system, the Ho^{3+} dopant concentration is typically higher in Pr^{3+}-coped systems to increase the rate of energy transfer from Ho^{3+} to Pr^{3+}. Table VII lists the rate parameters and fiber parameters that were used in the calculation that are relevant to reported core pumped [6] and cladding pumped [2] Ho^{3+}, Pr^{3+}-co-doped ZBLAN fiber laser experiments. In a similar way to the cascade system, for the WI case, the rate parameters W_{11}, W_{22}, W_{30} as well as W_{40} were estimated to be 12 times lower than those determined from bulk glasses [13].

TABLE VII
VARIABLE SPECTROSCOPIC PARAMETERS AND FIBER PARAMETERS USED IN THE SIMULATIONS

Variable parameters				
	[6]		[2]	
	SI	WI	SI	WI
W_{11} [10^{-23}m^3 s^{-1}]	2.8	0.23	2.8	0.23
W_{22} [10^{-23}m^3 s^{-1}]	25	2.08	25	2.08
W_{30} [10^{-23} m^3 s^{-1}]	5	0.42	5	0.42
W_{40} [10^{-23} m^3 s^{-1}]	4.2	0.35	4.2	0.35
N_{Ho} [m^{-3}]	4.125×10^{26}		4.125×10^{26}	
N_{Pr} [m^{-3}]	4.125×10^{25}		3.437×10^{25}	
r_{core} [m]	7.5×10^{-6}		5×10^{-6}	
r_{core} [m]	52×10^{-6}		52×10^{-6}	
NA	0.13		0.2	
L [m]	3		5	
α_s [m^{-1}]	23×10^{-3}		23×10^{-3}	
b_1/b_2	1/0.4		1/0.24	
W_1 [m^3 s^{-1}]	1.58×10^{-22}		1.5×10^{-22}	
W_2 [m^3 s^{-1}]	6×10^{-24}		5.5×10^{-22}	
λ_p [m]	1100×10^{-9}		1150×10^{-9}	
λ_s [m]	2.86×10^{-6}		2.94×10^{-6}	
σ_{GSA} [m^2]	2.85×10^{-27}		1.85×10^{-25}	
σ_{ESA1} [m^2]	0.1×10^{-25}		0.4×10^{-25}	
σ_{ESA2} [m^2]	0.12×10^{-25}		0.15×10^{-25}	
σ_{se} [m^2]	4.5×10^{-25}		1.3×10^{-25}	
R_{p1}	0		0	
R_{p2}	0.04		0.04	
R_{s1}	0.98		0.98	
R_{s2}	0.04		0.04	

TABLE VIII
COMPARISON OF THE SIMULATED RESULTS AND EXPERIMENT RESULTS IN [6] AND [2]

	[6]			[2]		
	SI	WI	Exp.	SI	WI	Exp.
η_s [%]	26	29	29	27	32.7	32
P_{th} [mW]	202	32	28	510	120	15

Fig. 10 (a) and (b) shows the measured and calculated output power as a function of the launched pump power for the experimental arrangements. The experimental and calculated slope efficiencies and threshold pump power are listed in Table VIII. The calculations from the model agree well with the measurements except the calculated threshold for [2], thus validating the model for the Ho^{3+}, Pr^{3+}-co-doped system and the use of the WI rate parameters.

The rates of GSA, ET_1, ET_2, ESA_1, ESA_2, ETU_1, ETU_2, CR_1, CR_2, and SE_{21} at the output end to the fiber were

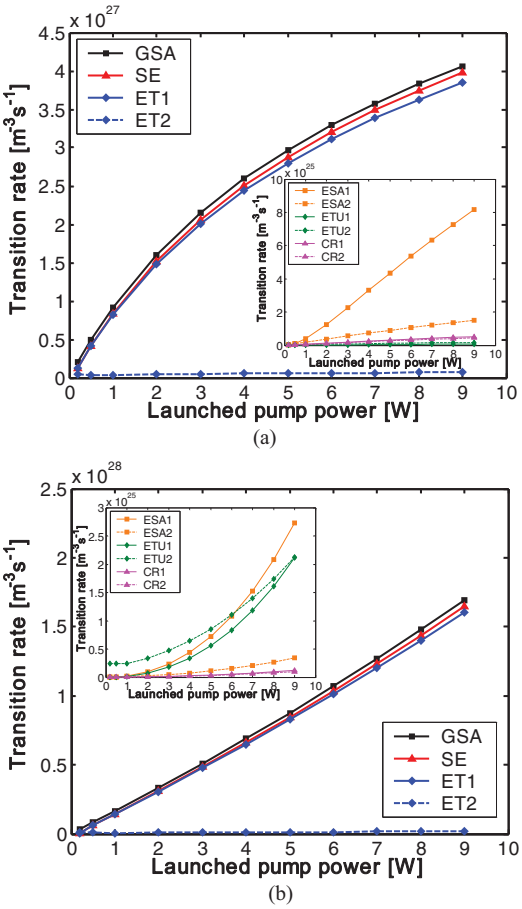

Fig. 11. Calculated rates of GSA, ET_1, ET_2, ESA_1, ESA_2, ETU_1, ETU_2, CR_1, CR_2, and SE_{21} at the output end of the fiber as a function of launched pump power for (a) core-pumped and (b) cladding-pumped Ho^{3+}, Pr^{3+}-co-doped system.

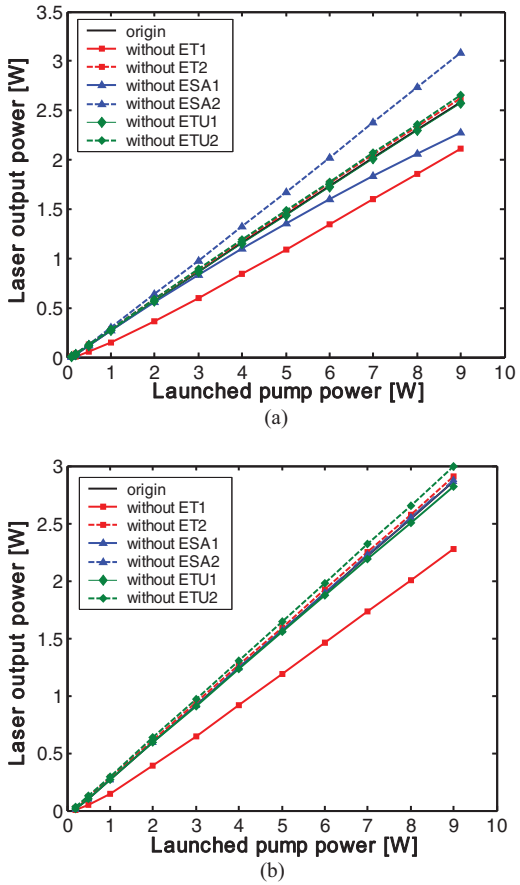

Fig. 12. Calculated output power as a function of the launched pump power without ET_1, ET_2, ESA_1, ESA_2, ETU_1, and ETU_2 for (a) core pumped and (b) cladding pumped Ho^{3+}, Pr^{3+}-co-doped system.

calculated as a function of the launched pump power for the core pumped and cladding pumped arrangements, as shown in Fig. 11(a) and (b). It is observed that GSA increases significantly with increasing launched pump power and no ground state bleaching occurs. Owing to the fast quenching of the population density located in the $^5I_7$ level as a result of the high rate of ET_1, the rates of ESA_1 and ETU_1 from this level are much smaller than GSA. The rates of ESA_2 and ETU_2 from the $^5I_8$ level were also much smaller than GSA owing to the relatively high rate of SE. For the core pumped system, the rates of ESA_1 and ESA_2 were much higher than the rates of ETU_1 and ETU_2 as a result of high pump intensity.

To understand the effects from ET_1, ET_2, ESA_1, ESA_2, ETU_1, and ETU_2 on laser performance in core pumped or cladding pumped systems, the input-output curves without ET_1, ET_2, ESA_1, ESA_2, ETU_1 or ETU_2 were compared, as shown in Fig. 12(a) and (b). For the core pumped arrangement, the slope efficiencies without ET_1, ET_2, ESA_1, ESA_2, ETU_1 or ETU_2 were 23.9%, 29.4%, 25.8%, 34.7%, 29% or 29.8%, respectively, which suggests that ET_1 and ESA_1 lead to an increase in the population inversion enhancing the slope efficiency, and ET_2, ESA_2 and ETU_2 processes lead to a decrease in the population inversion reducing the slope efficiency. Obviously ET_1, ESA_1 and ESA_2 are the main factors affecting the slope efficiency in the core-pumped arrangement, while ETU_1 makes a negligible contribution. For the cladding pumped arrangement, the slope efficiencies without ET_1, ET_2, ESA_1, ESA_2, ETU_1 or ETU_2 were 26.2%, 33%, 32.8%, 32.7%, 32.7%, 32% or 33.7%, respectively, indicating ESA_1 and ESA_2 have a negligible contribution as a result of their low rate values. ET_1 and ETU_1 enhance the slope efficiency while ET_2 and ETU_2 reduce the slope efficiency. ET_1 and ETU_2 are the main factors affecting the performance of lasers using the cladding-pumped arrangement.

C. Singly Resonant Ho^{3+}-Doped ZBLAN Fiber Lasers

It has been demonstrated [11, 12] that the $^5I_6 \rightarrow ^5I_7$ transition can lase without cascading or co-doping with Pr^{3+} as a result of depletion the $^5I_7$ laser level from ESA_1 or ETU_1. To better understand the role of the ESA and ETU processes on the operation of singly Ho^{3+}-doped ZBLAN fiber lasers systems, we numerically simulated two Ho^{3+}-doped ZBLAN fiber lasers: (1) a fiber laser employing a fiber doped with 0.5 mol.% Ho^{3+} and core pumped at 1175 nm [11] and (2) a fiber laser employing a fiber doped with 4.2 mol.% Ho^{3+} and core pumped at 1100 nm [12]. Table IX lists the rate parameters that were used in the calculation and the measured and calculated slope efficiencies and thresholds. Note that the laser wavelength in [11] was not measured, which is assumed

TABLE IX
VARIABLE PARAMETERS AND CALCULATED CHARACTERISTICS FROM THE NUMERICAL MODEL COMPARED WITH PREVIOUS EXPERIMENT DATA, WHICH ARE TAKEN FROM THE LITERATURE [11] AND [12]

Variable parameters				
	[11]		[12]	
	SI	WI	SI	WI
W_{11} [10^{-23}m^3 s^{-1}]	1	0.083	2.8	0.23
W_{22} [10^{-23} m^3 s^{-1}]	8	0.667	32	2.67
W_{30} [10^{-23} m^3 s^{-1}]	2	0.167	5.2	0.43
W_{40} [10^{-23} m^3 s^{-1}]	0.4	0.033	6	0.5
N_{Ho} [m^{-3}]	4.125×10^{26}		5.775×10^{26}	
r_{core} [m]	7.5×10^{-6}		6.5×10^{-6}	
NA	0.245		0.16	
L [m]	1.33		2	
α_s [m^{-1}]	23×10^{-3}		50×10^{-3}	
b_1/b_2	1/0.3		1/0.24	
λ_p [m]	1175×10^{-9}		1100×10^{-9}	
λ_s [m]	2.9×10^{-6}		2.92×10^{-6}	
σ_{GSA} [m^2]	0.95×10^{-25}		2.85×10^{-27}	
σ_{ESA1} [m^2]	1×10^{-25}		0.1×10^{-25}	
σ_{ESA2} [m^2]	0.1×10^{-25}		0.12×10^{-25}	
σ_{se} [m^2]	2.5×10^{-25}		1.5×10^{-25}	
R_{p1}	0		0	
R_{p2}	0.04		0.04	
R_{s1}	0.98		0.98	
R_{s2}	0.04		0.04	
Simulated results				
	SI	WI	Exp.	SI	WI	Exp.
η_s [%]	17	32	45	7.3	16.3	4.7
P_{th} [mW]	190	85	46	990	450	420

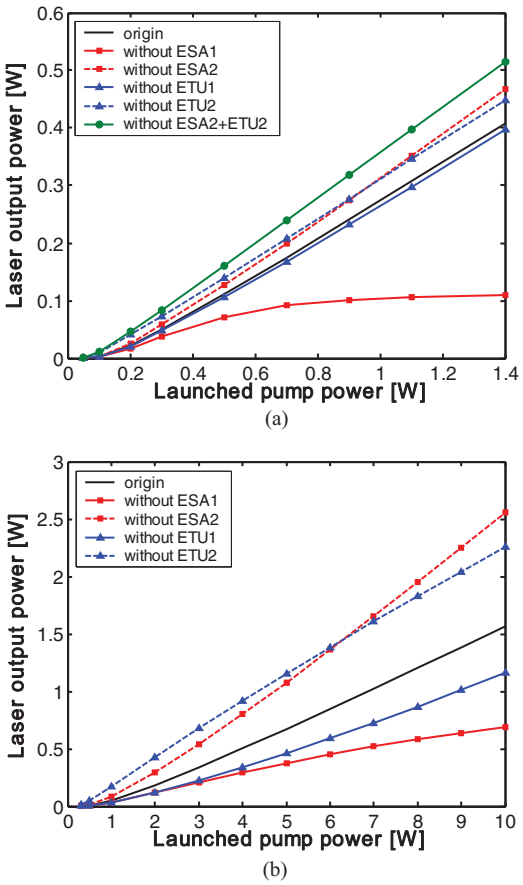

Fig. 13. Calculated output power as a function of the launched pump power without ESA_1, ESA_2, ETU_1, and ETU_2 for core pumped (a) low concentration and (b) high concentration singly Ho^{3+}-doped system.

to be 2.9 μm in the calculations according to the measured spectrum in [9] with the same fiber length.

For the first case, the calculated threshold using WI parameters is close to the experimental result; using the SI parameters the threshold is much higher. The calculated slope efficiency using the WI parameters is lower by 13% than the experiment result, which was higher than the Stokes limit of 40%. To find the discrepancy, the laser characteristic without ESA_1, ESA_2, ETU_1, or ETU_2 were compared, as shown in Fig. 13(a). It is observed that ETU_1 and ESA_1 contribute positively to the performance of laser, particularly ESA_1. As is now established, ESA_2 and ETU_2 are detrimental to the performance. The calculated slope efficiencies without ESA_1, ESA_2, ETU_1 or ETU_2 were 18.2%, 35.3%, 30% and 33.6%, respectively and the maximum calculated slope efficiency is 38.5% when ESA_2 and ETU_2 were switched off, indicating that the measured slope efficiency of 45% is probably wrong.

For the second case, the calculated threshold using WI parameters is close to the experiment result; the SI parameters predict a higher threshold. The calculated slope efficiency using the WI parameters is higher than the experiment result a factor that may relate to the quality of the fiber or ion clustering; a condition not measured directly but is thought to reduce the slope efficiency [18]. The laser characteristic without ESA_1, ESA_2, ETU_1, or ETU_2 were compared, as shown in Fig. 13(b). The calculated slope efficiencies without ESA_1, ESA_2, ETU_1 or ETU_2 are 7.5%, 26.7%, 12% and 23.4%, respectively; indicating that ESA_1 is still the main favorable process in core pumped highly concentrated singly Ho^{3+} doped systems.

IV. DISCUSSION

This investigation is the first attempt at modeling the Ho^{3+}-doped ZBLAN fiber laser designed for emission in the 3-μm region of the infrared spectrum. Good agreement between the model and experiments was achieved in most of cases except two: the cladding pumped cascade fiber laser and the high concentration singly Ho^{3+}-doped fiber laser. Given the number of spectroscopic studies of Ho^{3+}-doped fluoride glasses that have been carried out, we believe that the disagreement does not relate to an unknown energy transfer process. The Ho^{3+}-doped fluoride glass system is a fairly well understood system with most of the parameters relating to the photon and ion-ion interactions known. The substantial difference between the calculated and experimental slope efficiencies does require more investigation and we are currently repeating the experiment reported in [8] and [12]. In addition we are numerically modeling direct upper laser level pumping of the $^5I_7$ level for emission at 2.1 μm in both core and cladding pumped

arrangements in an effort to fully understand the Ho^{3+}-doped fluoride glass system.

There are a number of outcomes from this investigation that have improved our understanding of Ho^{3+}-doped ZBLAN fiber lasers including:

1) In core pumped low (<1 mol.%) dopant concentration cascade Ho^{3+}-doped fiber lasers, ETU_1 and ETU_2 make a negligible contribution to both transitions. ESA_2 reduces the slope efficiencies of both $^5I_6 \rightarrow {}^5I_7$ and $^5I_7 \rightarrow {}^5I_8$ transitions while ESA_1 is only detrimental to the slope efficiency of the $^5I_7 \rightarrow {}^5I_8$ laser transition.
2) In cladding-pumped cascade systems, the ESA_1 and ESA_2 processes make a negligible contribution as a result of low pump intensity. ETU_2 increases the threshold of both $^5I_6 \rightarrow {}^5I_7$ and $^5I_7 \rightarrow {}^5I_8$ transitions while ETU_1 increases the threshold of the $^5I_7 \rightarrow {}^5I_8$ transition. ETU_2 is detrimental to both transitions and ETU_1 contributes to the $^5I_6 \rightarrow {}^5I_7$ transition but is detrimental to the $^5I_7 \rightarrow {}^5I_8$ transition.
3) In the core pumped Ho^{3+}, Pr^{3+}-co-doped system, ET_1, and ESA_1 contribute to and ET_2, ESA_2 and ETU_2 have a detrimental effect on the $^5I_6 \rightarrow {}^5I_7$ laser transition. ET_1, ESA_1 and ESA_2 are the main factors affecting the slope efficiency, while ETU_1 makes a negligible contribution.
4) In cladding pumped Ho^{3+}, Pr^{3+}-co-doped systems, ESA_1 and ESA_2 make a negligible contribution. ET_1 and ETU_1 contribute to and ET_2 and ETU_2 have a detrimental effect on the $^5I_6 \rightarrow {}^5I_7$ transition. ET_1 and ETU_2 are the main factors affecting the performance of laser.
5) In core pumped singly Ho^{3+}-doped system, ESA_1 and ETU_1 contribute to and ESA_2 and ETU_2 have a detrimental effect on the $^5I_6 \rightarrow {}^5I_7$ laser transition. ESA_1 is the main factor depopulating the $^5I_7$ level.

V. Conclusion

We have reported a comprehensive theoretical model for core pumped and cladding pumped cascaded Ho^{3+}-doped, Ho^{3+}, Pr^{3+}-co-doped and single transition Ho^{3+}-doped fluoride fiber lasers. The model was validated when good agreement was achieved with most of the results from previously reported experiments that have varying fiber and resonator parameters. In a similar way to the erbium fluoride fiber laser system, best agreement with experimental results occurred when the rate parameters for energy transfer measured from bulk glasses were scaled down. A significant disagreement, however, between the calculations and recent experimental result of the slope efficiency of cladding-pumped cascaded systems was observed. The interionic processes that primarily affect the performance each fiber laser system have been identified allowing for the design of future Ho^{3+}-doped fluoride fiber lasers. This work is the first step towards the optimization of the Ho^{3+}-doped fluoride glass fiber laser system.

Acknowledgment

The authors acknowledge financial support from the Australian Research Council, Australia, through the Discovery Projects and the receipt of a Queen Elizabeth II Fellowship.

References

[1] S. Tokita, M. Murakami, S. Shimizu, M. Hashida, and S. Sakabe, "Liquid-cooled 24 W mid-infrared Er:ZBLAN fiber laser," *Opt. Lett.*, vol. 34, no. 20, pp. 3062–3064, 2009.
[2] S. D. Jackson, "High-power and highly efficient diode-cladding-pumped holmium-doped fluoride fiber laser operating at 2.94 μm," *Opt. Lett.*, vol. 34, no. 15, pp. 2327–2329, 2009.
[3] Y. H. Tsang, A. E. El-Taher, T. A. King, and S. D. Jackson, "Efficient 2.96 μm dysprosium-doped fluoride fiber laser pumped with a ND:YAG laser operating at 1.3 μm," *Opt. Lett.*, vol. 29, no. 2, pp. 334–336, 2004.
[4] D. Faucher, M. Bernier, G. Androz, N. Caron, and R. Vallee, "20 W passively cooled single-mode all-fiber laser at 2.8 μm," *Opt. Lett.*, vol. 36, no. 7, pp. 1104–1106, 2011.
[5] M. Bernier, D. Faucher, N. Caron, and R. Vallée, "Highly stable and efficient erbium-doped 2.8 μm all fiber laser," *Opt. Exp.*, vol. 17, no. 19, pp. 16941–16946, 2009.
[6] S. D. Jackson, "Single-transverse-mode 2.5-W holmium-doped fluoride fiber laser operating at 2.86 μm," *Opt. Lett.*, vol. 29, no. 4, pp. 334–336, 2004.
[7] D. Hudson, E. Magi, L. Gomes, and S. D. Jackson, "1 W diode-pumped tunable Ho^{3+}, Pr^{3+}-doped fluoride glass fibre laser," *Electron. Lett.*, vol. 47, no. 17, pp. 985–986, 2011.
[8] J. Li, D. D. Hudson, and S. D. Jackson, "High-power diode-pumped fiber laser operating at 3 μm," *Opt. Lett.*, vol. 36, no. 18, pp. 3642–3644, 2011.
[9] T. Sumiyoshi, H. Sekita, T. Arai, S. Sato, M. Ishihara, and M. Kikuchi, "High-power continuous-wave 3- and 2-μm cascade Ho^{3+}:ZBLAN fiber laser and its medical applications," *IEEE J. Sel. Topics Quantum Electron.*, vol. 5, no. 4, pp. 936–943, Aug. 1999.
[10] T. Sumiyoshi and H. Sekita, "Dual-wavelength continuous-wave cascade oscillation at 3 and 2 μm with a holmium-doped fluoride-glass fiber laser," *Opt. Lett.*, vol. 23, no. 23, pp. 1837–1839, 1998.
[11] D. V. Talavera and E. B. Mejia, "Holmium-doped fluoride fiber laser at 2950 nm pumped at 1175 nm," *Laser Phys.*, vol. 16, no. 3, pp. 436–440, 2006.
[12] S. D. Jackson, "Singly Ho^{3+}-doped fluoride fibre laser operating at 2.92 μm," *Electron. Lett.*, vol. 40, no. 22, pp. 1400–1401, Oct. 2004.
[13] A. F. H. Librantz, S. D. Jackson, F. H. Jagosich, L. Gomes, G. Poirier, S. J. L. Ribeiro, and Y. Messaddeq, "Excited state dynamics of the Ho^{3+} ions in holmium singly doped and holmium, praseodymium-codoped fluoride glasses," *J. Appl. Phys.*, vol. 101, no. 2, pp. 123111-1–123111-9, Jun. 2007.
[14] M. Gorjan, M. Marincek, and M. Copic, "Role of interionic processes in the efficiency and operation of erbium-doped fluoride fiber lasers," *IEEE J. Quantum Electron.*, vol. 47, no. 2, pp. 262–273, Feb. 2011.
[15] A. Guhur and S. D. Jackson, "Efficient holmium-doped fluoride fiber laser emitting 2.1 μm and blue upconversion fluorescence upon excitation at 2 μm," *Opt. Exp.*, vol. 18, no. 19, pp. 20164–20169, 2010.
[16] R. Li, J. Li, L. Shterengas, and S. D. Jackson, "Highly efficient holmium fibre laser diode pumped at 1.94 μm," *Electron. Lett.*, vol. 47, no. 19, pp. 1089–1090, Sep. 2011.
[17] A. F. H. Librantz, S. D. Jackson, L. Gomes, S. J. L. Ribeiro, and Y. Messaddeq, "Pump excited state absorption in holmium-doped fluoride glass," *J. Appl. Phys.*, vol. 103, no. 2, pp. 023105–023113, 2011.
[18] J. Li, K. Duan, Y. Wang, W. Zhao, J. Zhu, Y. Guo, and X. Lin, "Modeling and effects of ion pairs in high-concentration erbium-doped fiber lasers," *J. Modern Opt.*, vol. 55, no. 6, pp. 447–458, 2008.

Jianfeng Li (M'10) received the B.S. degree in applied physics from Sichuan University, Chengdu, China, and the M.S. and Ph.D. degrees in optical engineering from the School of Physics, Institute of Nano-Optics, Sichuan University, in 2003, 2005, and 2008, respectively.

He joined the School of Optoelectronic Information, University of Electronic Science and Technology of China, Chengdu, in 2008, where he became an Associate Professor in 2009. In 2011, he joined the Center for Ultrahigh Bandwidth Devices for Optical Systems, School of Physics, University of Sydney, Sydney, Australia, as a Visiting Scientist. His current research interests include midinfrared fiber lasers, fiber sensors, and nonlinear fiber optics.

Laércio Gomes was born in Brazil, on April 2, 1950. He received the Ph.D. degree from the University of São Paulo, São Paulo, Brazil, in 1985, for the research of comprehensive study of OH- photodissociation in alkali halide crystals and the luminescence quenching effects of F centers correlated to the OH- molecular ions.

He was subsequently involved in the investigation of the mechanism of nonradiative energy transfer between trivalent rare earth ions in solids. Since 1990, he has been with the Center for Laser and Applications, IPEN-CNEN-SP, São Paulo, researching rare-earth-doped crystal fluoride and glasses to develop new laser materials.

Stuart D. Jackson (M'11) received the B.Sc. and B.Sc. (hons.) degrees from the University of Newcastle, Newcastle, Australia, and the Ph.D. degree from Macquarie University, Macquarie Park, Australia, in 1989, 1990, and 1996, respectively.

He joined the Center for Lasers and Applications, Macquarie University, in 1990. In 1995, he joined the Laser Photonics Group, University of Manchester, Manchester, U.K., and initiated research into high-power fiber lasers. In 1999, he joined the Optical Fiber Technology Center, University of Sydney, Sydney, Australia, where he became a Senior Research Fellow and Technical Manager of silica fiber fabrication. In 2009, he joined the School of Physics, University of Sydney, as a Queen Elizabeth II Fellow funded by the Australia Research Council (ARC) Project "Mid-Infrared Photonics" of the Centre for Ultrahigh Bandwidth Devices for Optical Systems, funded by the ARC Centre of Excellence. His current research interests include diode-pumped solid-state lasers, spectroscopy, nonlinear optics, and integrated optics.